JUSTC

Article

http://justc.ustc.edu.cn

Received: March 26, 2024; Accepted: May 14, 2024

Effect of substrate temperature and oxygen plasma treatment on the properties of magnetron-sputtered CdS for solar cell applications

Runxuan Zang, Haolin Wang, Xiaoqi Peng, Ke Li, Yuehao Gu, Yizhe Dong, Zhihao Yan, Zhiyuan Cai, Huihui Gao, Shuwei Sheng, Rongfeng Tang, and Tao Chen ✉

Department of Materials Science and Engineering, School of Chemistry and Materials Science, University of Science and Technology of China, Hefei 230026, China

✉Correspondence: Tao Chen, E-mail: tchenmse@ustc.edu.cn

Graphical abstract

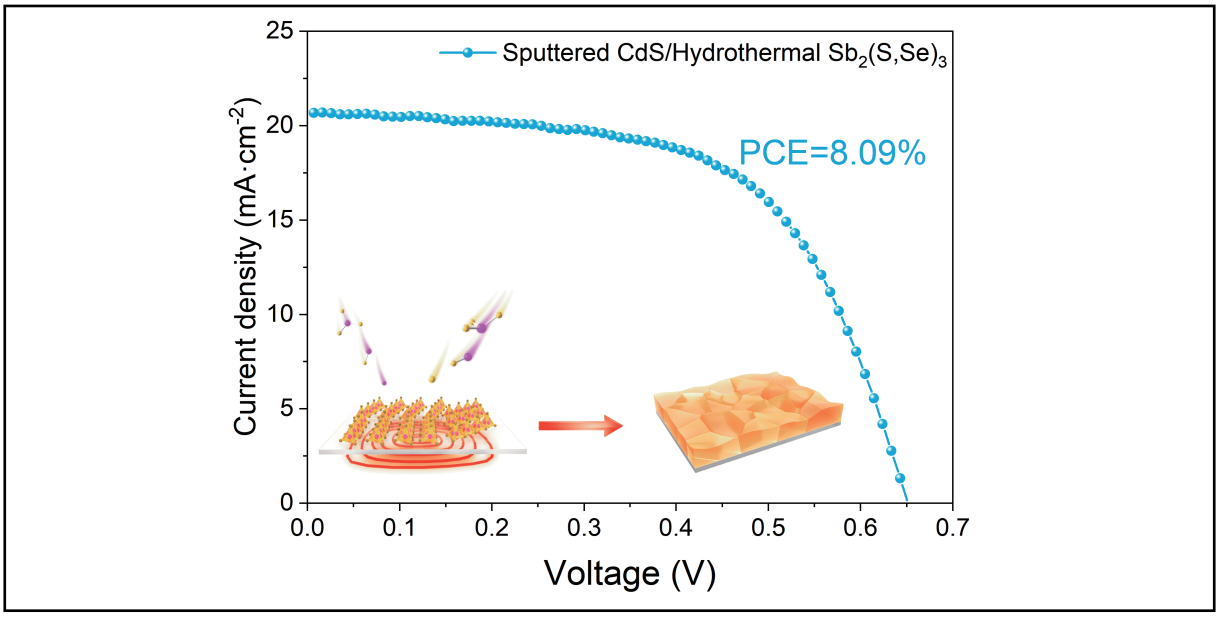

Under substrate heating conditions, the CdS thin film prepared by magnetron sputtering has a flat and dense morphology with enhanced crystallinity.

Public summary

- Substrate heating was used during the sputtering process to improve the quality of the CdS thin film.
- A higher crystallinity and smoother surface as well as a good energy level matching between the CdS and $Sb_2(S,Se)_3$ absorber layers are achieved.
- Oxygen plasma treatment was used to treat the CdS layer to reduce Se diffusion during the annealing process, which improves the J_{SC} and power conversion efficiency of solar cells.
- A solar cell device with a power conversion efficiency of 8.09% is achieved, which is the highest among all antimony chalcogenide solar cells based on a sputtered CdS window layer.

Citation: Zang R X, Wang H L, Peng X Q, et al. Effect of substrate temperature and oxygen plasma treatment on the properties of magnetron-sputtered CdS for solar cell applications. *JUSTC*, **2024**, 54(6): 0604. DOI: 10.52396/JUSTC-2024-0048

JUSTC

Article

http://justc.ustc.edu.cn

Received: March 26, 2024; Accepted: May 14, 2024

Effect of substrate temperature and oxygen plasma treatment on the properties of magnetron-sputtered CdS for solar cell applications

Runxuan Zang, Haolin Wang, Xiaoqi Peng, Ke Li, Yuehao Gu, Yizhe Dong, Zhihao Yan, Zhiyuan Cai, Huihui Gao, Shuwei Sheng, Rongfeng Tang, and Tao Chen ✉

Department of Materials Science and Engineering, School of Chemistry and Materials Science, University of Science and Technology of China, Hefei 230026, China

✉Correspondence: Tao Chen, E-mail: tchenmse@ustc.edu.cn

Cite This: *JUSTC*, **2024**, 54(6): 0604 (12pp)

Read Online

Abstract: Cadmium sulfide (CdS) is an n-type semiconductor with excellent electrical conductivity that is widely used as an electron transport material (ETM) in solar cells. At present, numerous methods for preparing CdS thin films have emerged, among which magnetron sputtering (MS) is one of the most commonly used vacuum techniques. For this type of technique, the substrate temperature is one of the key deposition parameters that affects the interfacial properties between the target film and substrate, determining the specific growth habits of the films. Herein, the effect of substrate temperature on the microstructure and electrical properties of magnetron-sputtered CdS (MS-CdS) films was studied and applied for the first time in hydrothermally deposited antimony selenosulfide ($Sb_2(S,Se)_3$) solar cells. Adjusting the substrate temperature not only results in the design of the flat and dense film with enhanced crystallinity but also leads to the formation of an energy level arrangement with a $Sb_2(S,Se)_3$ layer that is more favorable for electron transfer. In addition, we developed an oxygen plasma treatment for CdS, reducing the parasitic absorption of the device and resulting in an increase in the short-circuit current density of the solar cell. This study demonstrates the feasibility of MS-CdS in the fabrication of hydrothermal $Sb_2(S,Se)_3$ solar cells and provides interface optimization strategies to improve device performance.

Keywords: magnetron sputtering; CdS; substrate heating; plasma treatment; $Sb_2(S,Se)_3$; thin film; solar cell

CLC number: TB383; TM914.4 **Document code:** A

1 Introduction

Cadmium sulfide (CdS) plays an important role as a window layer in thin film photovoltaic technology, especially in chalcogenide solar cells, including $Cu(In,Ga)Se_2$ (CIGS), $Cu_2ZnSn(S,Se)_4$ (CZTSSe) and CdTe[1–3]. The easy bonding chemical nature of CdS and proper lattice constant that matches well with usual photovoltaic (PV) absorber materials make it an ideal window layer. When used in the superstrate configuration, the high thermal and chemical stability of CdS allows for multiple methods to deposit a high-quality absorber layer onto this substrate. Antimony chalcogenides, including antimony selenide (Sb_2Se_3), antimony sulfide (Sb_2S_3) and antimony selenosulfide ($Sb_2(S,Se)_3$), have emerged as attractive light-harvesting materials for solar cells owing to their simple chemical composition, high phase stability, low toxicity and abundant element storage[4–8]. Among all the available window layers, CdS is the most popular because of its ability to fabricate highly efficient solar cell devices.

CdS has been deposited in a variety of ways, including chemical bath deposition[4, 9–11], closed space sublimation[12], thermal evaporation[13], spin coating[14], molecular beam epitaxy[15], atomic layer deposition[16] and magnetron sputtering (MS)[17–24]. As a third-generation vacuum thin film deposition technology, magnetron sputtering has many advantages, including a high deposition rate, thorough material coverage, high purity and adhesion of the deposited films, and high uniformity on large-area substrates[25]. Compared with the traditional CBD method, magnetron-sputtered CdS shows greater environmental friendliness, good control of film thickness and greater uniformity on large substrates (see Supplementary Note 1 in Supporting information). All these advantages, especially the ability to fabricate large-area thin films[26], make it suitable for industrial application in synthesizing CdS for solar cells[17–24, 27]. The magnetron-sputtered CdS (MS-CdS) typically uses reactive sputtering in environments containing a mixture of O_2 and Ar gases to improve its electrical properties. The MS-CdS thin film has also been applied in antimony chalcogenide solar cells. Guo et al.[18] reported that using 2% O_2 in sputtering gas not only increased the bandgap of CdS thin films from approximately 2.4 eV to 2.6 eV, increasing the transmittance of the Sb_2Se_3 active layer, but also improved the grain size and crystal orientation of Sb_2Se_3. Moreover, the band alignment at the CdS/Sb_2Se_3 interface changes from a “cliff”-like structure to a “spike”-like structure, contributing to an increase in the power conversion effi-

DOI: 10.52396/JUSTC-2024-0048

JUSTC, **2024**, 54(6): 0604

ciency from 3.59% to 7.01%. However, there is an intrinsic problem of uncontrollability with the use of O_2 during sputtering, as mass flow control is based on the closed-loop control principle. Fluctuations might occur in the gas flow during the sputtering process, and a change of only approximately 1% in the O_2 concentration can lead to a change of 1.5% in the power conversion efficiency (PCE). The use of substrate heating during the deposition process can reduce the impact of gas flow fluctuations on the photovoltaic performance of the device and improve the device efficiency. However, the specific explanations for this improvement have not yet been reported[18,19,21,22,24].

Herein, for the first time, magnetron-sputtered CdS was used in a hydrothermally fabricated $Sb_2(S,Se)_3$ solar cell with a superstrate structure of fluorine-doped tin oxide (FTO)/CdS/$Sb_2(S,Se)_3$/2,2',7,7'-tetrakis(N,N-di-p-methoxyphenylamine)-9,9'-spirobifluorene (Spiro-OMeTAD)/Au. The effect of the substrate heating temperature on the electrical properties of CdS and the improvement in device photovoltaic performance can be attributed to the improved crystallinity and flatter surface of CdS together with a more favorable band alignment with the $Sb_2(S,Se)_3$ layer. We found that a change of approximately 50 °C near the optimal temperature only results in a change of approximately 1% in the PCE, which demonstrates a much greater reproducibility than that of the method using O_2 during sputtering. In addition, a post-oxygen plasma treatment was conducted to reduce the parasitic absorption of CdS, improve the J_{SC}, and achieve a PCE of 8.09%. This study provides an effective strategy and new understanding of interface passivation to improve the efficiency of antimony selenosulfide solar cells.

2 Experimental section

2.1 Ingredient information

fluorine-doped tin oxide (FTO) glass (15 mm×20 mm) was obtained from Liaoning YingKou Libra New Energy Technology Co., Ltd. FTO is specified as GD-H8 with a square resistance of 6–10 $\Omega\cdot sq^{-1}$. $C_4H_4KO_7Sb\cdot 0.5H_2O$ and $Na_2S_2O_3\cdot 5H_2O$ were obtained from Sinopharm. CH_4N_2Se with a purity of 98% was obtained from Sigma–Aldrich. 2,2',7,7'-Tetrakis[N,N-di(4-methoxyphenyl)amino]-9,9'-spirobifluorene (Spiro-OMeTAD) was obtained from Yingkou Youxuan Trade Co., Ltd. Acetonitrile (C_2H_3N), lithium bis(trifluoromethylsulfonyl) imide (Li-TFSI), and 4-tert-butylpyridine (tBP) were obtained from J&K. All solvents and other materials were used without additional purification. The CdS target used in magnetron sputtering was purchased from Hebei Qinbang New Materials Technology Co., Ltd. The size of the target was 7 cm×20 cm.

2.2 Magnetron sputtering of CdS

FTO substrates were cleaned ultrasonically in FTO detergent diluted with a deionized water–deionized water–ethanol sequence, each lasting for 40 min. Thereafter, the substrates were dried under N_2 gas flow. Before sputtering, the FTO substrates were cleaned using a mixture of Ar/O_2 plasma at an RF power of 20 W for 15 min to remove organic residues. The RF sputtering device was manufactured by Wuhan PDVACUUM Technology Company (PD-400 with a customized two-chamber design). The base pressure was 5×10^{-4} Pa. Prior to deposition and presputtering, the substrates must undergo a preheating process to achieve better solar cell performance. RF power sources were purchased from Advanced Energy. The RF power was set to 25 W with approximately 0–1 W reverse sputtering power. Pure Ar gas was chosen as the working gas. The gas flow was set to 30 sccm, and the pressure in the sputtering chamber was approximately 1.5 Pa. The presputtering step lasted for approximately 10 min, and the sputtering process lasted for approximately 29 min. The optimized substrate heating temperature was chosen to be 200 °C, with other temperatures (room temperature, 150 °C, 250 °C) used for comparison.

2.3 Posttreatment of sputtered CdS

After the sputtering process, the CdS must undergo several post-treatments. Under basic conditions, only $CdCl_2$ spin coating and ambient air annealing are needed. Two extra steps or changes are required for further improvements in the PCE. For the chloride spin coating, the basic condition was a $CdCl_2$ solution, which used $CdCl_2\cdot 2.5H_2O$ as the $CdCl_2$ source and ethanol as the solvent, and the concentration was 5 mg/mL. For the mixed chloride solution, the solution had a $CdCl_2$ concentration of 2.5 mg/mL and a $SbCl_3$ concentration of 15 mg/mL. Ethanol was still used as the solvent. The CdS was annealed at 400 °C for 10 min in ambient air after chloride spin coating. Oxygen plasma treatment was conducted after the ambient air annealing process. The air pressure was set to approximately 80 Pa, and the power level was set to high power. 15 min was the optimal condition.

2.4 Fabrication of $Sb_2(S,Se)_3$ thin films

$Sb_2(S,Se)_3$ was deposited using a hydrothermal method as described in a previous report[10]. In a 100 mL beaker, 80 mL of deionized water was added to 0.5342 g of APT (antimony potassium tartrate) as an antimony source. The mixture must first be stirred to achieve a clear solution before adding other reactants. Then, 80 mg of NH_4F was added to the APT solution under stirring conditions. Stirring was continued until the solution was transferred to the autoclave. After approximately 1 min, 1.5884 g of STS (sodium thiosulfate) was added to the above solution. After another 5 min, 50 mg of selenourea was added to the above solution. Before the addition of selenourea, the solution was slightly yellow. After the addition of selenourea, the solution gradually turned. The final solution was transferred into a 50 mL autoclave with CdS sputtered on FTO/glass attached to a glass slide facing down[4]. The autoclave was placed in a baking oven at 135 °C for 2 h. After cooling to room temperature (RT) naturally, the sample substrates were rinsed with deionized water and ethanol and blow-dried with nitrogen gas. Finally, the as-grown $Sb_2(S,Se)_3$ films were annealed at 375 °C for 10 min in a N_2 atmosphere to enhance the crystallinity.

2.5 Device fabrication

The hole transport material was fabricated according to a previously reported method[15]. First, 36.6 mg of Spiro-OMeTAD was dissolved in a mixed solution containing 1 mL of

DOI: 10.52396/JUSTC-2024-0048
JUSTC, **2024**, 54(6): 0604

chlorobenzene, 14.5 μL of 4-tert-butyl pyridine and 9.5 μL of Li-TFSI solution (520 mg·mL^{-1} Li-TFSI in acetonitrile). The as-prepared Spiro-OMeTAD solution was spin-coated onto the $Sb_2(S,Se)_3$ sample at 3000 r/min for 30 s. The spin-coated Spiro-OMeTAD was annealed at 105 °C for 10 min in ambient air as an oxidation process. Finally, the device was finished by thermal evaporation of a Au (70 nm) film as a metal electrode.

2.6 Characterization of films and devices

The surface morphology and cross-sectional scanning electron microscopy (SEM) images of $Sb_2(S,Se)_3$ and CdS were observed using cold field-emission SEM (Hitachi SU8220) and Shockley emission SEM (Zeiss G450). Energy dispersive spectroscopy (EDS) was performed using an Oxford EDS detector as an attachment in the SEM instrument. The analysis software Aztec was also developed by the Oxford instrument. The crystal structures of $Sb_2(S,Se)_3$ and CdS thin films were characterized by XRD (D/Max-rA) with Cu Kα radiation (λ = 1.5406 Å). The ultraviolet–visible absorption spectra were obtained using a UV–visible spectrophotometer (UV–vis DRS, SOLID 3700). UPS measurements were carried out on a Thermo ESCALAB 250XI. To eliminate residual pollutants on the surface, Ar ion sputtering was used to clean the surface prior to the measurements. The sputtering depth for CdS was 2 nm, and that for $Sb_2(S,Se)_3$ was 10 nm. The EIS measurements were performed on an electrochemical workstation (Zahner Mess System PP211) with frequencies ranging from 1 Hz to 1 MHz at a bias potential of −0.6 V in the dark. The capacitance–voltage (C–V) curves were obtained from the same electrochemical workstation at RT with a frequency of 10 kHz. The AC amplitude was 5 mV. The DC bias voltage was changed from −0.1 to 0.8 V. The voltage–current density characteristics of the $Sb_2(S,Se)_3$ devices were determined using a Keithley 2400 sourcemeter unit under AM 1.5G illumination at 1000 W·m^{-2} with an Oriel Sol 3A and a Japan solar simulator. The active area of the electrode was 0.105 cm^2. The EQE (Newport QuantX-300) was measured using a single-source illumination system (halogen lamp) combined with a monochromator. Atomic force microscopy (AFM) was performed using a Bruker Dimension icon. The transient absorption spectra (TASs) of $Sb_2(S,Se)_3$ films with different amounts of sputtered CdS were obtained using a Helios setup in which a nondegenerate pump-probe configuration was applied to probe the transient dynamics (8000 to 0 ps). An optical parametric amplifier (OPerA Solo) was pumped by a 1-kHz regenerative amplifier (Coherent Libra, 800 nm, 50 fs, 4 mJ). Frequency doubling of the fundamental output by a mode-locked Ti-sapphire oscillator (Coherent Vitesse, 80 MHz) was used to generate pump pulses. The white light generated by a sapphire plate was used to generate probe pulses. To ensure sufficient light transmittance, the $Sb_2(S,Se)_3$ film growth time was reduced from 120 min to 35 min, with a thickness of approximately 40 nm.

3 Results and discussion

3.1 Effect of substrate heating temperature

The microstructure and electrical properties of CdS sputtered at RT or at substrate heating temperatures of 150 °C, 200 °C and 250 °C were investigated. X-ray diffraction (XRD) was used to determine the crystal structure of CdS. The standard thickness of CdS (60 nm) used in the device usually exhibits a weak XRD peak intensity, causing its peak response to be confused by background noise (see Supporting information Fig. S2). Therefore, a 240 nm thick CdS sample was deposited for XRD analysis (Fig. 1). Considering that the CdS sputtered on FTO displays the real status of the crystal, while the CdS sputtered on glass displays the accurate position of the peak without confusion with the FTO peak, two results are displayed. In addition, all the samples were subjected to $CdCl_2$ solution spin coating and ambient air annealing before being characterized.

The XRD results for CdS sputtered on a glass substrate are shown in Fig. 1a. Only the (002), (110), (103), and (004) diffraction peaks corresponding to hexagonal-phase CdS are detected, indicating that the CdS film prepared by magnetron sputtering is a pure hexagonal-phase crystal. The same phenomenon was observed when FTO was used as the substrate (Fig. 1b). Considering that the position of the (002) peak coincides with that of the FTO peak, as well as the influence of substrate properties on the crystal orientation of the deposited films, we performed grazing-incidence X-ray diffraction

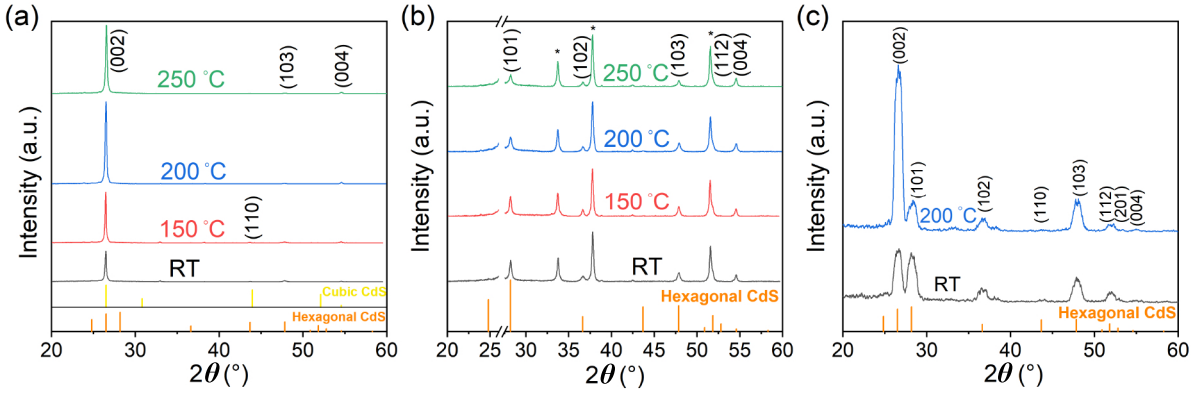

Fig. 1. X-ray diffraction (XRD) pattern of the sputtered CdS thin film. The deposition time was 2 h, four times the standard CdS growth time. (a) CdS sputtered on a glass substrate at different temperatures. (b) CdS sputtered on an FTO substrate. The positions of the FTO diffraction peaks are labeled with asterisks. (c) Grazing incidence XRD (GIXRD) result of CdS sputtered on an FTO substrate. The incident angle is 0.4°, and no FTO substrate peaks are found.

DOI: 10.52396/JUSTC-2024-0048
JUSTC, **2024**, 54(6): 0604

(GIXRD) characterization (Fig. 1c). As shown in Fig. 1c, an increase in the intensity of the (002) peak is observed under substrate heating conditions compared with that of the CdS film deposited at RT, and higher temperatures are more favorable for the growth of the (002) crystal plane, indicating that substrate heating helps to improve the crystallinity of the sputtered CdS film.

Scanning electron microscopy (SEM) characterization was conducted to investigate the surface morphology of the CdS particles sputtered before and after ambient air annealing (Fig. 2). The CdS films studied here were treated with a 5 mg/mL $CdCl_2$ ethanol solution and then annealed at 400 °C in ambient air for 10 min. As shown in the SEM image, the sputtered film is composed of small CdS particles with diameters less than 50 nm that are covered directly on the FTO substrate. CdS sputtered at different temperatures has similar nanoparticle sizes and shapes. After annealing in ambient air, the size of the nanoparticles increases to 50–100 nm and masks the morphology of the FTO substrate, contributing to a decrease in the surface roughness and an increase in the crystallinity. This morphological change is to some extent caused by the spin-coated $CdCl_2$ solution, as $CdCl_2$ acts as a flux to induce the recrystallization of CdS during postannealing treatment[28,29].

Generally, the growth of thin films consists of two processes: deposition and diffusion[30]. For the deposition of these films, the sputtering parameters are the same, so the deposition process of the incident particles is similar. The main influence of substrate heating is the diffusion of Cd and S atoms on the substrate surface, which can be depicted by the diffusion coefficient obtained from the following equation[31]:

$$D = \nu_0 \exp\left(\frac{-E}{k_B T}\right), \tag{1}$$

where ν_0 is the jump frequency and E is the diffusion activation energy, which typically amounts to tenths of eV. Therefore, higher temperatures will lead to larger diffusion coefficients, while lower temperatures will lead to smaller diffusion coefficients. At RT, the diffusion coefficient is low, and when atoms collide with the substrate, they will immediately stay at that position, with little opportunity to form an ordered arrangement to increase the crystallinity. In contrast, substrate heating can provide more energy for atoms to overcome intermediate states, thereby improving the crystallinity of CdS films. Although the postannealing process helps atoms diffuse to the correct lattice position, the crystallinity of the thin film still depends on the original position of the CdS clusters[32]. However, when the temperature is too high, the reduction in the free energy retained in the correct lattice position cannot effectively constrain the ability of atoms to escape from that position, resulting in a decrease in crystallinity. Moreover, AFM revealed that substrate heating reduced the surface roughness (Rq) of CdS from 41.3 nm (at RT) to 36.6 nm (at 150 °C). A further increase in temperature had almost no effect on Rq, which was approximately 36.0 nm at 200 °C and 250 °C (see Supporting information Fig. S5). This is because the concave position has a lower energy, and atoms tend to migrate to these areas to decrease the surface energy on the substrate (see Supporting information Fig. S6)[33].

Furthermore, the optical properties of CdS were characterized via ultraviolet–visible (UV–Vis) absorption spectroscopy (see Supporting information Fig. S7). The CdS films deposited at RT, 150 °C, 200 °C and 250 °C were measured to have the same band gap of approximately 2.35 eV. However, all the films exhibit strong absorption in the wavelength range lower than 520 nm, thereby reducing the light absorption of the absorber layer. Therefore, a postprocessing method to reduce parasitic absorption is proposed, which will be discussed in Section 3.2.

Subsequently, $Sb_2(S,Se)_3$ films prepared by a hydrothermal method were deposited on the sputtered CdS and annealed at 350 °C for 10 min[10]. The XRD results (Fig. 3a) indicate that all the light absorber layers have orthorhombic Sb_2S_3 structures (PDF#42-1393). Specifically, the diffraction peaks shift toward lower angles due to the substitution of S atoms by Se atoms with larger atomic radii. In addition, the $Sb_2(S,Se)_3$ films grown on CdS prepared at different heating temperatures all exhibit flat and dense morphologies (Fig. 3c, d). Notably, heating the substrate increased the average grain size from 473 nm (RT) to 597 nm (200 °C), as shown in Fig. 3b. This result confirms the high quality of $Sb_2(S,Se)_3$

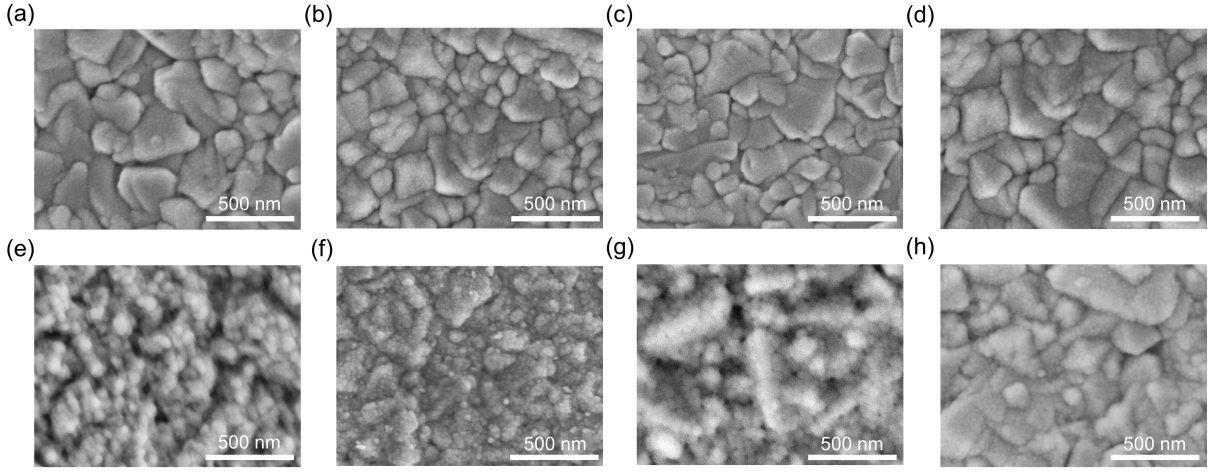

Fig. 2. SEM image of sputtered CdS. The first row shows sputtered CdS without ambient air annealing. The second row shows sputtered CdS with $CdCl_2$ spin coating and ambient air annealing posttreatment. The four columns show CdS sputtered at RT, 150 °C, 200 °C and 250 °C from left to right.

DOI: 10.52396/JUSTC-2024-0048
JUSTC, **2024**, 54(6): 0604

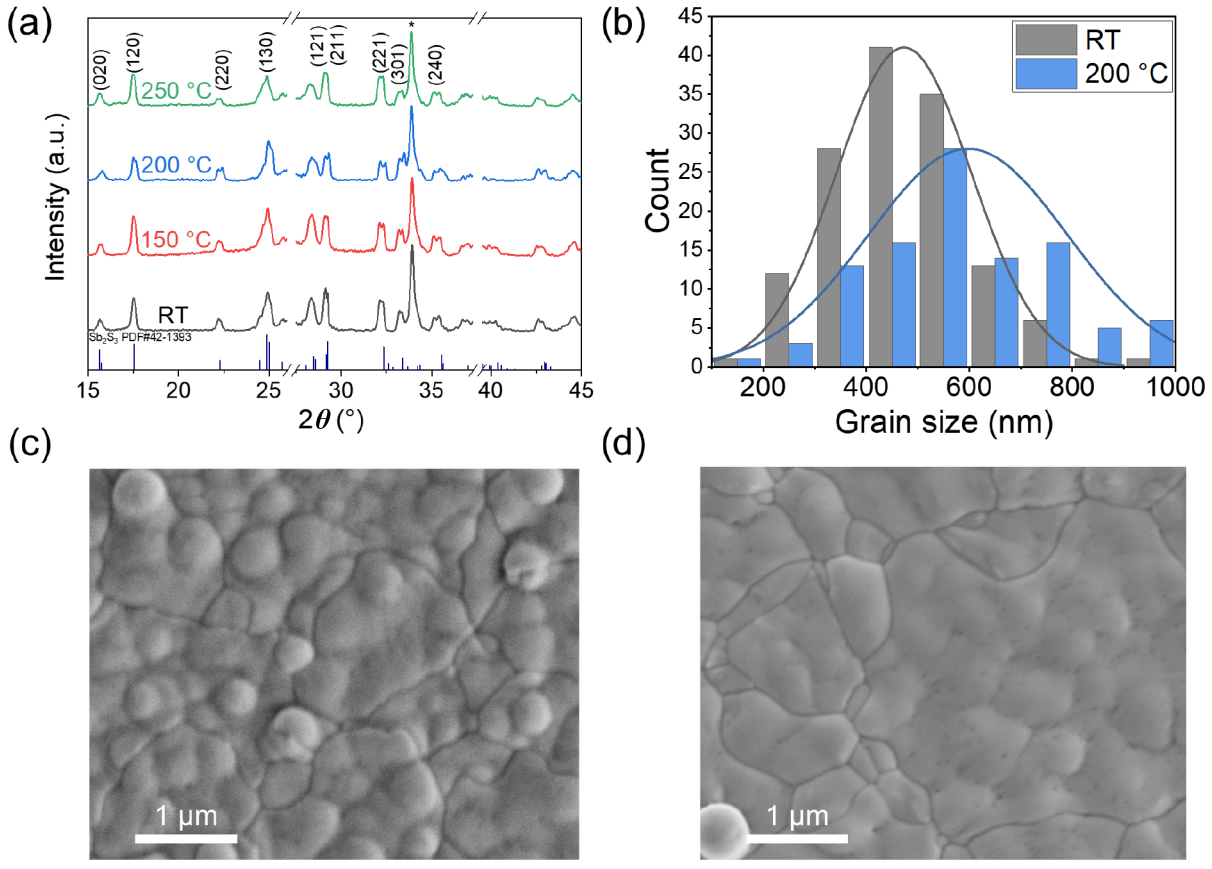

Fig. 3. Characterization of $Sb_2(S,Se)_3$ thin films grown on sputtered CdS. (a) XRD pattern of the $Sb_2(S,Se)_3$ thin film. (b) Statistics on the grain size of the $Sb_2(S,Se)_3$ thin film. SEM image of a $Sb_2(S,Se)_3$ thin film (c) grown on RT-sputtered CdS and (d) grown on 200 °C-sputtered CdS.

films grown on magnetron-sputtered CdS, especially those on CdS prepared at a substrate heating temperature of 200 °C (see Supporting information Fig. S8).

To understand the energy level arrangement between the CdS and $Sb_2(S,Se)_3$ layers, ultraviolet photoelectron spectroscopy (UPS) measurements were conducted to determine their valance band maximum (VBM), Fermi level (E_f), and conduction band minimum (CBM). As shown in Fig. 4a and b, the E_f values for CdS prepared under RT (RT-CdS) and heated (HT-CdS) conditions are measured to be −4.18 eV and −4.17 eV, respectively, and the differences between E_f and the VBM are 2.12 eV and 1.89 eV, respectively. Thus, the VBMs for RT-CdS and HT-CdS are calculated to be −6.32 eV and −6.06 eV, respectively, and the CBMs are −3.98 eV and −3.71 eV, respectively. Moreover, the energy levels of the $Sb_2(S,Se)_3$ absorber layer are extracted from the UPS results, with corresponding CBM, VBM, and E_f values of −3.84 eV, −5.34 eV and −4.15 eV, respectively (Fig. 4c). The energy level alignment of the $Sb_2(S,Se)_3$ solar cell devices was obtained (Fig. 4d, e). Notably, the RT-sputtered CdS/$Sb_2(S,Se)_3$ shows a "cliff"-like interface, while the heat-prepared CdS substrate forms a "spike"-like interface with $Sb_2(S,Se)_3$, with a ΔE_C of approximately 0.13 eV. Generally, a "spike" peak with a ΔE_C of 0.2 eV is beneficial for reducing the chance of carrier recombination, which is helpful for improving device efficiency[34]. Therefore, the improved band alignment between the substrate-heated CdS and $Sb_2(S,Se)_3$ can facilitate efficient carrier transport in a solar cell.

To investigate the effect of magnetron-sputtered CdS on the photovoltaic characteristics of $Sb_2(S,Se)_3$ solar cells, superstrate devices with a glass/FTO/sputtered CdS/$Sb_2(S,Se)_3$/Spiro-OMeTAD/Au configuration were assembled. For the convenience of discussion, the devices based on CdS prepared at RT, 150 °C, 200 °C and 250 °C are labeled the RT device, 150 °C device, 200 °C device, and 250 °C device, respectively. As shown in the current density–voltage (J–V) curves recorded under AM 1.5 G simulated sunlight (Fig. 5a), substrate heating significantly improved all the photovoltaic parameters of the device compared to those of the RT device. In particular, when CdS was prepared at a substrate temperature of 200 °C, the PCE increased from 4.76% (RT device) to 7.53%, the short-circuit current density (J_{SC}) increased from 18.61 mA·cm^{-2} to 19.41 mA·cm^{-2}, the open-circuit voltage (V_{OC}) increased from 608 mV to 632 mV, and the fill factor (FF) increased from 43.60% to 61.39% (Table 1). The cross-sectional SEM image of the 200 °C device is shown in Fig. S11 (see the Supporting information), corresponding to thicknesses of ~60, 300, 100, and 70 nm for the CdS, $Sb_2(S,Se)_3$, Spiro-OMeTAD and Au back contact layers, respectively. The improved device performance is mainly caused by the increased crystallinity of CdS. A lower heating temperature is not sufficient for better crystallization of CdS, so the improvement in device efficiency is lower for CdS deposited at 150 °C (PCE, 6.96%) than for CdS deposited at 200 °C. When the heating temperature increases to 250 °C, the corresponding device also shows a decrease in the PCE compared

DOI: 10.52396/JUSTC-2024-0048
JUSTC, **2024**, 54(6): 0604

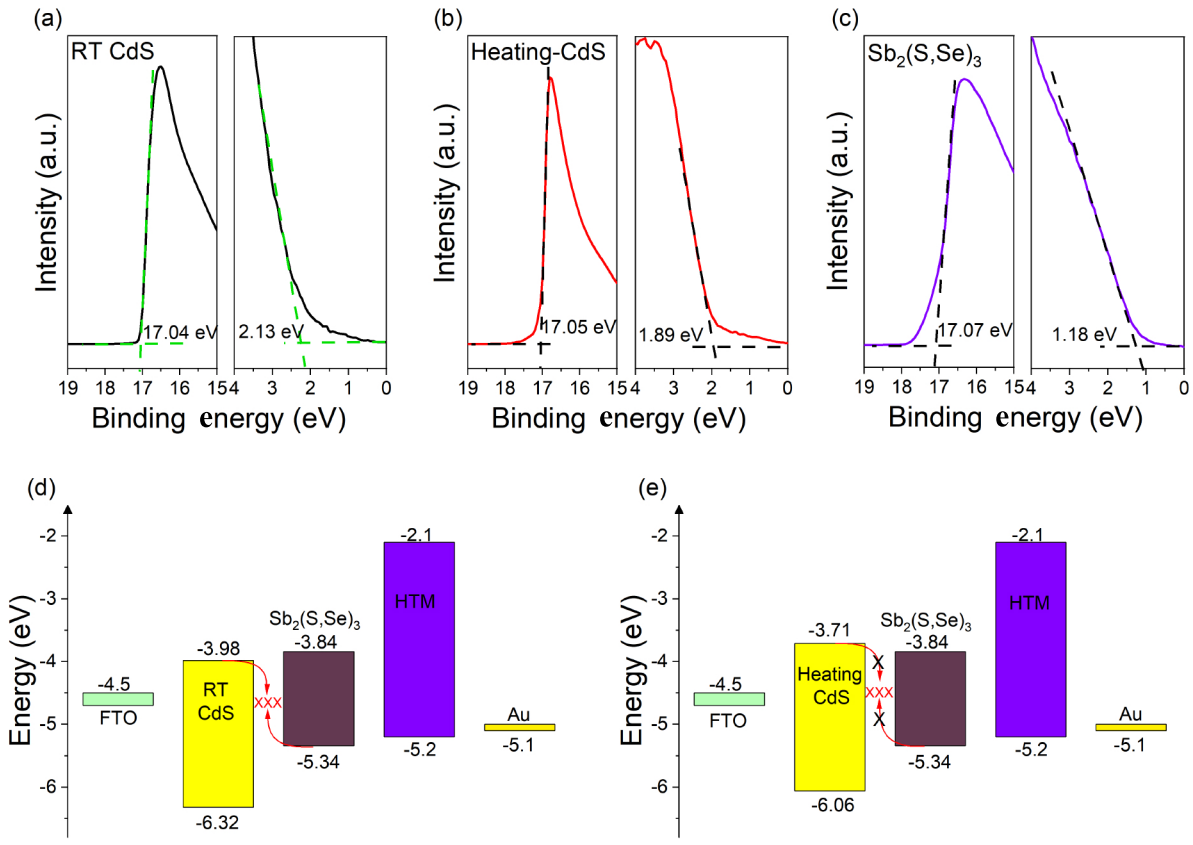

Fig. 4. UPS spectra of (a) RT-sputtered CdS, (b) substrate heat-sputtered CdS and (c) $Sb_2(S,Se)_3$ thin films. (d, e) Band alignment diagram of the $Sb_2(S,Se)_3$ solar cell devices.

Table 1. Champion device parameters of $Sb_2(S,Se)_3$ solar cells grown on sputtered CdS under different heating conditions.

Condition	V_{OC} (mV)	J_{SC} (mA·cm^{-2})	FF (%)	η (%)	J_0 (mA·cm^{-2})	n	G_{sh} (S·cm^{-2})	R_s (Ω·cm^2)
RT	586	18.61	43.60	4.76	9.06E−03	8.42	0.070	1.158
150 °C	608	19.17	59.71	6.96	1.29E−04	2.07	0.044	0.584
200 °C	632	19.41	61.39	7.53	8.95E−06	1.73	0.011	0.491
250 °C	624	18.49	61.51	7.10	2.66E−05	1.80	0.019	0.625

to that of the 200 °C device, with a PCE of approximately 7.1%, which is mainly caused by the decrease in the J_{SC} (18.49 mA·cm^{-2}). Combined with the structural influence of CdS (Fig. 2), we found that posttreatment with $CdCl_2$ and high-temperature annealing at 400 °C did not cause significant changes in the morphology of the 250 °C-CdS film. This phenomenon indicates that the CdS film prepared at 250 °C is too stable, which is not conducive to subsequent defect passivation operations by $CdCl_2$ spin coating treatment, resulting in enhanced light absorption of CdS and a corresponding increase in parasitic absorption of the device, as shown in the external quantum efficiency (EQE) spectra in Fig. 5d. The statistical results of the PCE, V_{OC}, J_{SC}, and FF further confirm the effect of substrate heating of CdS on improving the photovoltaic performance of the devices (Fig. 5b, c, e, f).

The charge transport and recombination mechanism of the devices were studied through a series of electrochemical characterizations. By recording the dark J–V response of the device (Fig. 6a), it was observed that the device based on the HT-CdS film consists of three parts from low voltage to high voltage, namely, the Shunt resistance (R_{sh}) effected or leak current region, the exponential diode behavior region and the series resistance (R_s) effected region[35]. The heating devices all exhibit three distinct zones, while the RT device shows blurred zones, indicating that the RT device has not formed a benign diode structure due to the mismatched energy alignment between the CdS and $Sb_2(S,Se)_3$ layers. In addition, the reverse saturation current density (J_0) is derived by extrapolating the linear part of the log$J$–V curve, and the results are listed in Table 1. The J_0 of the 200 °C device is found to be lower (8.95×10^{-6} mA·cm^{-2}) than that of the 250 °C device (2.66×10^{-5} mA·cm^{-2}) and the 150 °C device (1.29×10^{-4} mA·cm^{-2}); in particular, it is several orders of magnitude lower than that of the RT device (9.06×10^{-3} mA·cm^{-2}). A de-

DOI: 10.52396/JUSTC-2024-0048
JUSTC, **2024**, 54(6): 0604

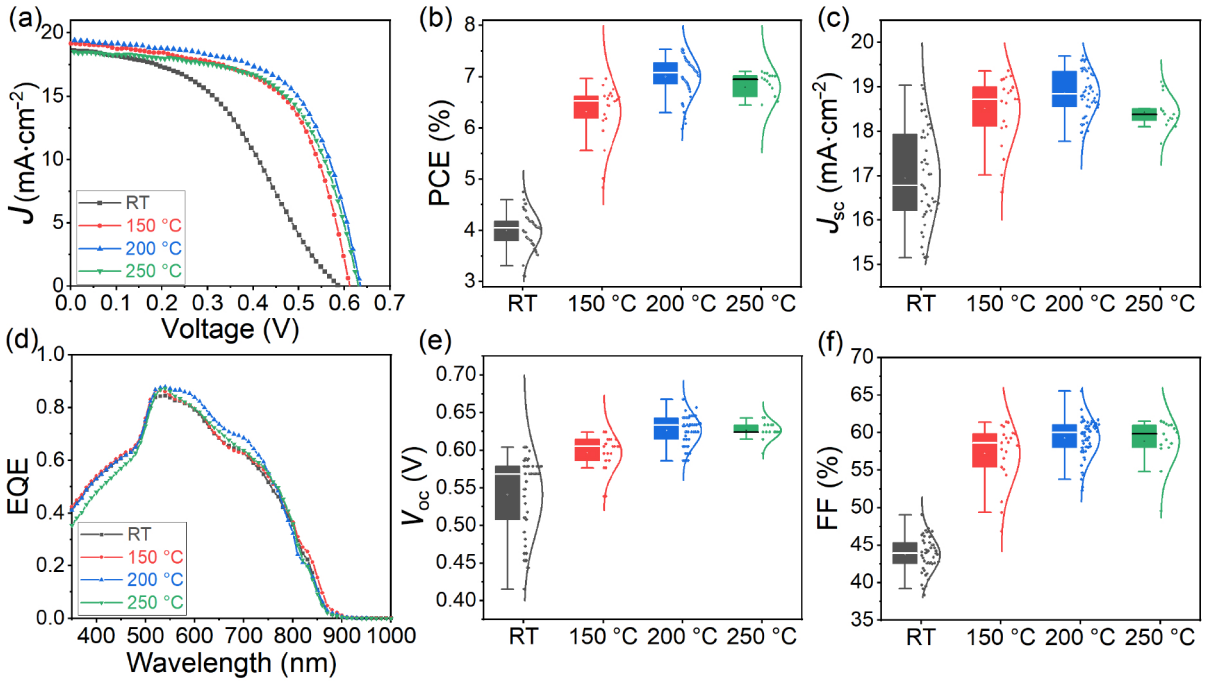

Fig. 5. Photovoltaic performance of the devices. (a) Current density–voltage (*J*–*V*) curves of $Sb_2(S,Se)_3$ solar cell devices grown on sputtered CdS under different substrate heating conditions. Statistical boxplots of the photovoltaic parameters (b) power conversion efficiency (PCE), (c) short-circuit current density (J_{SC}), (e) open-circuit voltage (V_{OC}), and (f) fill factor (FF) of the corresponding devices. (d) External quantum efficiency (EQE) spectra of the corresponding devices.

crease in J_0 indicates a decrease in the leakage current of the device. The ideality factor (n) of the devices was also calculated according to the reported equation[35–36], and the 200 °C device showed a significantly lower value (1.73) than the other three devices, indicating that the trap-assisted recombination of the device was effectively suppressed. In fact, an n value closer to 1 indicates a greater degree of inhibition for trap-assisted recombination. However, for the RT device, the n value is calculated to be 8.42. This value much larger than 2 is probably attributed to other physical effects, such as interface recombination and the Poole-Henkel high field effect[37–39], which also occurs in other antimony chalcogenide solar cell devices[39–41]. The extremely high n value indicates the poor current rectification characteristics of the RT device, resulting in an S-shaped *J*–*V* curve and poor device performance.

By plotting the dJ/dV vs V plot (Fig. 6b)[40–42], the Shunt conductance (G_{sh}) of the device is derived, which corresponds to the dJ/dV value at the lowest point of the curve. Compared with the other three devices, the 200 °C device shows the lowest shunt conductance (0.011 S·cm^{-2}) because the substrate heating temperature of 200 °C improves the uniformity and coverage of the deposited CdS film. Moreover, the series resistance (R_s) is obtained from the linear part of dV/dJ against the $(J+J_{SC})^{-1}$ curve. The CdS films deposited with substrate heating reduced the R_s from 1.158 Ω·cm^2 for the RT device to 0.584, 0.491 and 0.625 Ω·cm^2 for the 150 °C, 200 °C and 250 °C devices, respectively (Fig. 6c), which is consistent with the results obtained from the *J*–*V* curves recorded under illumination (see Supporting information Fig. S12)[40–43]. Obviously, the 200 °C device has the lowest series resistance, combined with the lowest G_{sh}, indicating that the 200 °C device has an improved heterojunction quality.

J–*V* curves measured under different light intensity irradiation conditions were used to investigate the carrier recombination state in the devices. The variations in V_{OC} and J_{SC} depending on light intensity are shown in Fig. 6d, e. ε and α are obtained from the slopes of the lines according to the following equations[44]:

$$V_{OC} = \frac{\varepsilon kT \ln(I)}{e} + constant, \tag{2}$$

$$J_{SC} = I^{\alpha}, \tag{3}$$

where e, k, T, ε and α are the elementary charge, Boltzmann constant, temperature, ideal factor and exponential factor, respectively. The 200 °C device is calculated to have a lower ε value (1.30) than the RT, 150 °C and 250 °C devices, with ε values of 1.82, 1.49 and 1.45, respectively. An ε close to 1 indicates the suppression of monomolecular Shockley-Read-Hall (SRH) recombination[4]. The smaller ε for devices based on substrate heat-deposited CdS indicates that trap-assisted recombination is effectively suppressed, especially in the 200 °C device. For α, a higher value indicates the suppression of bimolecular recombination[44]. Therefore, the higher α for the 200 °C device (0.879) than for the other three devices demonstrates its suppressed bimolecular recombination. The above results indicate the importance of substrate heating in improving the electron extraction ability of CdS, which is beneficial for reducing the carrier recombination of the device.

Electrochemical impedance spectroscopy (EIS) of the devices was conducted to characterize the carrier transport process. Fig. 6f presents the Nyquist plots and fitting equivalent electronic circuit of the devices, where the R_s and R_{REC}

DOI: 10.52396/JUSTC-2024-0048
JUSTC, **2024**, 54(6): 0604

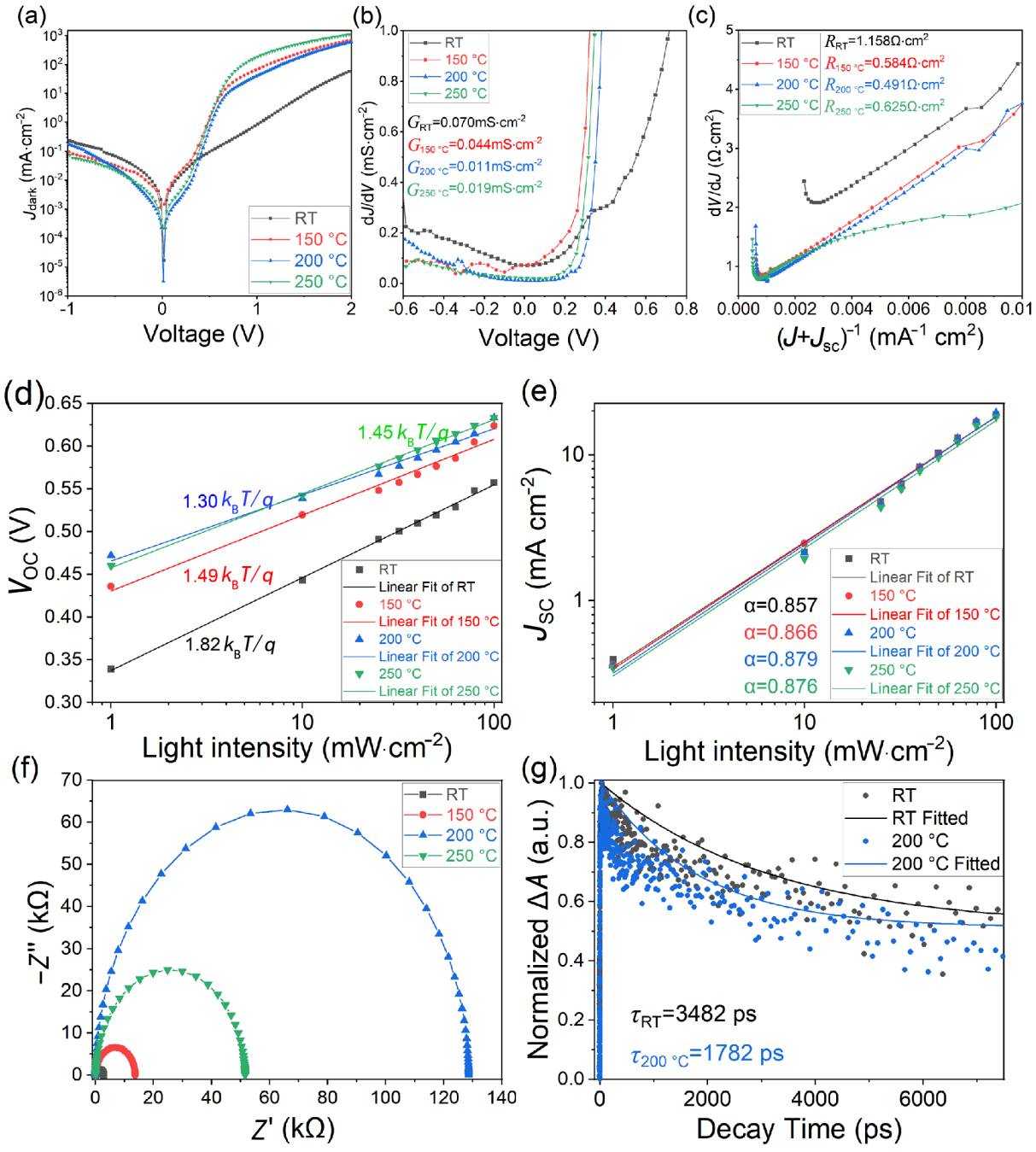

Fig. 6. Characterization of $Sb_2(S,Se)_3$ solar cell devices grown on sputtered CdS under different substrate heating conditions. Dark current results are shown in the first row with (a) *J*–*V* curve, (b) d*J*/d*V* versus voltage plot, and (c) d*V*/d*J* versus $(J+J_{SC})^{-1}$ plot. Here, the dark *J*–*V* data were measured starting at +3 V, so that $(J+J_{SC})^{-1}$ increased to approximately 0.002 mA^{-1}·cm^2. Under very high voltage conditions, the derivative increases, forming a tail at the end of the curve. However, this does not influence the analysis by using the well-defined linear part of the curve. The light intensity, electrochemical characterization and carrier transport kinetics of the devices are shown next. (d) Relation between V_{OC} and the logarithm of the incident light intensity. (e) Relation between J_{SC} and the incident light intensity. (f) Nyquist plots (under dark conditions at −0.60 V) of the devices. (g) Original data and fitted curves of transient decay kinetics monitored at 665 nm for $Sb_2(S,Se)_3$ films grown on sputtered CdS at RT and at 200 °C.

corresponding to the series and recombination resistance are extracted (see Supporting information Table S1)[4, 45]. Compared with RT-CdS, CdS deposited in the substrate temperature range of 150–250 °C improves the electrical properties of the device to varying degrees, especially CdS deposited at 200 °C, which decreases the R_s from 34.0 Ω to 8.3 Ω and increases the R_{REC} from 2.736 kΩ to 128.58 kΩ. This result indicates that the improved CdS layer promotes effective carrier transport within the device and reduces electron-hole recombination.

To further explore the effect of substrate heating conditions on carrier transport dynamics, we performed transient

DOI: 10.52396/JUSTC-2024-0048
JUSTC, **2024**, 54(6): 0604

absorption spectroscopy (TAS) characterization[46,47]. Here, time-resolved transient spectra in the range of 0–8000 ps were recorded. A 410 nm pulse laser was used to illuminate the FTO/CdS/$Sb_2(S,Se)_3$ samples containing RT-CdS, 150 °C-CdS, 200 °C-CdS and 250 °C-CdS. According to the TAS maps in Fig. S13 (see the Supporting information), two absorption peaks near 450 and 650 nm are detected, which are characteristic of CdS and $Sb_2(S,Se)_3$[42]. Positive signal and decay behavior are detected at wavelengths larger than 550 nm, providing information on carrier transport dynamics. The decay kinetics of the four films at a wavelength of 665 nm were extracted (Fig. 6g, Fig. S13b, c), and the kinetics curve was fitted by a biexponential decay model[4,46]. The fitting results indicate that the carrier decay of the 200 °C-device is faster, with an average decay time of approximately 1782 ps, while increasing to 3482, 1994 and 2773 ps for the RT-, 150 °C-, and 250 °C-devices, respectively. A faster decay means efficient electron transfer processes in the device, which reduces the probability of hole-electron recombination.

3.2 Effect of oxygen plasma treatment

Furthermore, prior to the deposition of $Sb_2(S,Se)_3$, the CdS films underwent oxygen plasma treatment (OPT). This treatment has been reported for CdS in Sb_2Se_3 solar cells, and its effect on the surface roughness of CdS and the growth of Sb_2Se_3 grains has been studied[48]. However, in this work, we achieved a reduction in parasitic absorption by treating CdS with oxygen plasma and increasing the J_{SC} of the device. For solar cells with CdS as the electron transport layer, parasitic absorption has always been an important factor affecting device performance improvement. In particular, when the absorber layer contains Se, the annealing process causes Se to diffuse into the CdS layer to form a CdSe interfacial layer with a narrow bandgap (1.7 eV), further intensifying parasitic absorption[10,49,50]. We validated this viewpoint by depositing $Sb_2(S,Se)_3$ films with different Se/S atomic ratios on CdS substrates (see Supporting information Fig. S14a).

Furthermore, to explore the impact of OPT on device performance, we focused on the effect of treatment time, which is an important regulatory parameter. Combined with the influence on device performance (see Supporting information Fig. S15), we find that an increase in the OPT time leads to an increase in the device PCE until 15 min, while the PCE gradually decreases thereafter. The changes in the PCE are mainly attributed to the changes in the J_{SC} because the impacts of OPT on the V_{OC} and FF are not significant. By recording the EQE response spectrum of the devices (Fig. S14b, c), it was revealed that OPT reduced the parasitic absorption of the device in the wavelength range of 300–550 nm, and the effect became more pronounced with increasing treatment time. When the OPT time reaches 30 min, the EQE slightly decreases, which is probably caused by the damage of plasma on CdS (the SEM image is shown in Supporting information Fig. S19). This kind of damage, to some extent, leads to a decrease in the ability to extract electrons, resulting in a decrease in J_{SC}. The integrated current density shows a trend similar to that of the statistics of the *J*–*V* results. The EQE spectra of the device under optimal OPT conditions (15 min) and the device without OPT are shown in Fig. 7b. The EQE results of devices based on CdS with and without OPT sputtering under different substrate heating conditions are also shown in Fig. S16 (see the Supporting information). For these devices, the EQE response in the parasitic absorption region significantly increased, verifying the universality of OPT.

To further elucidate the changes in the surface chemical state caused by oxygen plasma treatment, we conducted XPS analysis. We detected SO_4^{2-} and SO_3^{2-} on the surface of the CdS thin film after oxygen plasma treatment (see Supporting information Fig. S20). Since cadmium ions are the only cations that exist on the surface, we can conclude that $CdSO_4$ and $CdSO_3$ are formed. Previous work using O_2 as the working gas in magnetron-sputtered CdS in Sb_2Se_3 solar cells revealed the presence of SO_4^{2-} and SO_3^{2-}[22]. The bandgaps of $CdSO_4$ and $CdSO_3$ are larger than that of CdS. However, since oxygen plasma treatment is effective only for the surface of CdS, only the transmittance rate is slightly increased, but the bandgap derived from the UV–Vis results is unchanged.

At first glance, the increased transmittance rate might be the cause of the increase in the EQE response. However, by comparing the effects of OPT treatment on the parasitic absorption region of the EQE and the transmittance of CdS, it is found that the improvement in the EQE (approximately 8%) by this treatment is much greater than that in the transmittance of CdS (1%; see Supporting information Fig. S26b). Additionally, the increase in the EQE response only occurs in the parasitic absorption region instead of in the whole spectrum. Therefore, other factors should be considered in addition to the increase in transmittance. It can be inferred that the formation of $CdSO_4$ and $CdSO_3$ reduces Se diffusion during the absorber annealing process. Previous work has shown that the introduction of O_2 into the CdS sputtering process can effectively hinder Cd diffusion due to the formation of a CdS:O layer[22]. In fact, the diffusion of elements at the interface is mutual, and the presence of oxygen at the interface can reduce the overall diffusion of elements during the annealing process. As a result, the optimization of the substrate heating temperature and posttreatment process (see Supporting information Supplementary Note 3 and Figs. S22–S26) contributed to a superior device efficiency of 8.09% (the photovoltaic parameters extracted from the EQE and *J*–*V* curves are shown in Figs. S27, S28, and Table 2).

4 Conclusions

In conclusion, we demonstrate the effect of substrate heating on sputtered CdS in $Sb_2(S,Se)_3$ solar cells and propose two posttreatment methods for CdS layers. This proves that heating the substrate during sputtering results in higher crystallinity and lower surface roughness of CdS. The band alignment between CdS and the $Sb_2(S,Se)_3$ absorber layer is thus improved, forming a “spike”-like heterojunction, which facilitates carrier transport and reduces carrier recombination. In addition, two effective methods for treating CdS are proposed, and the effects of OPT are discussed in detail. The OPT operation forms a wide bandgap of CdOCl on the surface of CdS, which improves the transmittance of CdS. Moreover, the CdOCl layer reduces the diffusion of Se from

DOI: 10.52396/JUSTC-2024-0048
JUSTC, **2024**, 54(6): 0604

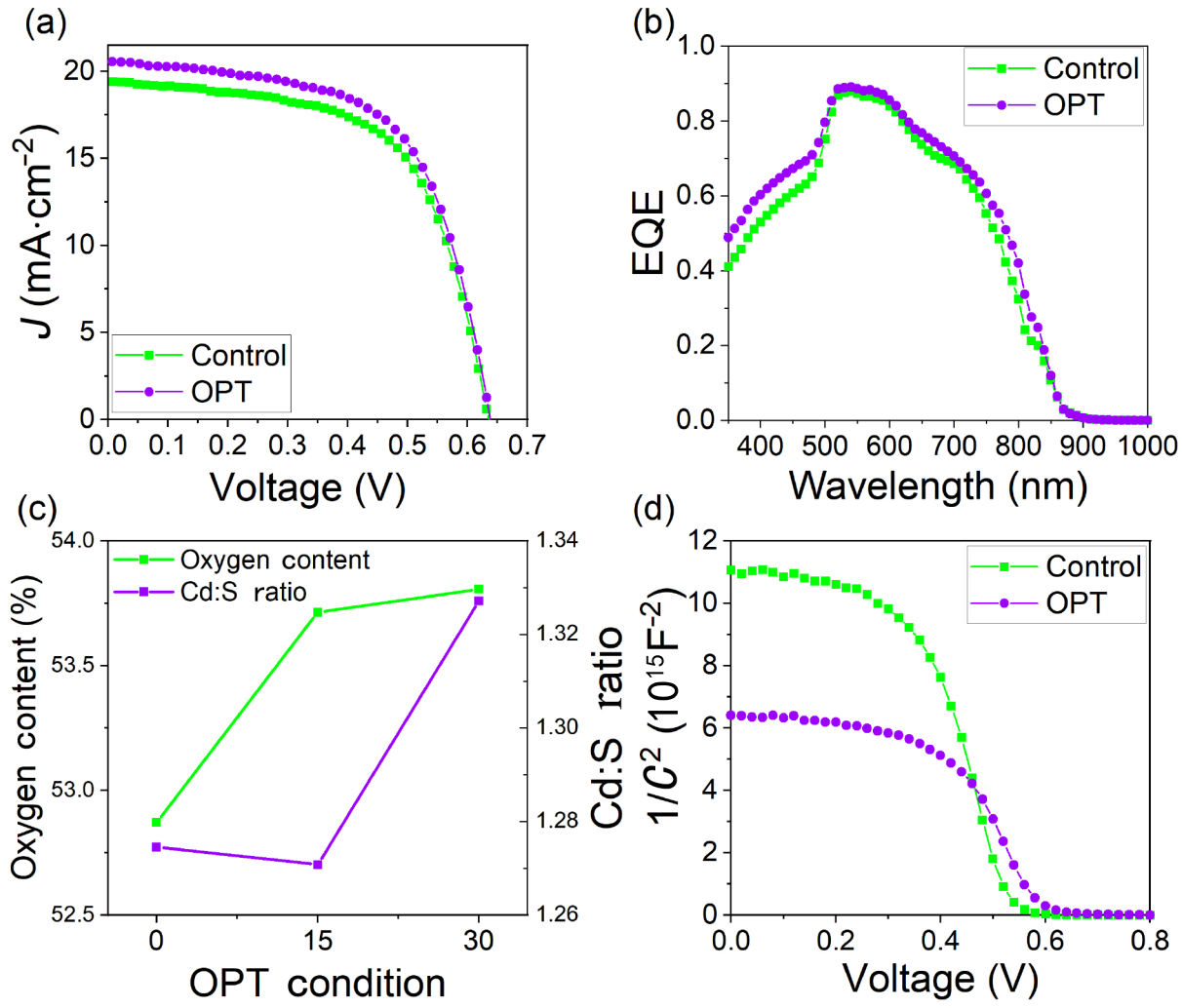

Fig. 7. Characterization related to oxygen plasma treatment of sputtered CdS. (a) Full-wavelength EQE spectra of devices with (15 min) and without oxygen plasma treatment (OPT). (b) Champion device efficiency with and without oxygen plasma treatment. (c) Oxygen content and Cd∶S ratio under different oxygen plasma treatment conditions. The results are based on EDS data. (d) The $1/C^2$–V curves of the devices recorded at a frequency of 100 kHz at RT in the dark.

Table 2. Champion device parameters of $Sb_2(S,Se)_3$ solar cells grown on 200 °C sputtered CdS with and without oxygen plasma treatment.

Devices	V_{OC} (mV)	J_{SC} (mA·cm^{-2})	FF (%)	PCE (%)
Control-device	632	19.41	61.39	7.53
OPT-device	643	20.67	60.89	8.09

the $Sb_2(S,Se)_3$ layer into the CdS layer, thereby reducing the parasitic absorption of CdS. Ultimately, the J_{SC} and the power conversion efficiency of the device are improved. This study proposes effective strategies to improve the quality of CdS electron transport materials as well as interfacial contact with $Sb_2(S,Se)_3$ light absorber layers on the basis of magnetron-sputtered CdS films, providing effective methods for improving the efficiency of $Sb_2(S,Se)_3$ solar cells.

Acknowledgements

This work was supported by the National Natural Science Foundation of China (22275180), the National Key Research and Development Program of China (2019YFA0405600), the Collaborative Innovation Program of Hefei Science Center, CAS, and the University Synergy Innovation Program of Anhui Province (GXXT-2023-031).

Conflict of interest

The authors declare that they have no conflict of interest.

Supporting information

The supporting information for this article can be found online at https://doi.org/10.52396/JUSTC-2024-0048. The supporting information includes 27 figures, three tables and three notes.

Biographies

Runxuan Zang is currently a master's student at the University of Science and Technology of China under the supervision of Prof. Tao Chen. His research mainly focuses on the application of magnetron sputtered CdS in antimony chalcogenide solar cells.

DOI: 10.52396/JUSTC-2024-0048
JUSTC, **2024**, 54(6): 0604

Tao Chen is a Professor in the Department of Materials Science and Engineering, University of Science and Technology of China. He received his Ph.D. degree in Chemistry from Nanyang Technological University in 2010. His research mainly focuses on metal chalcogenide solar cells and energy storage materials and devices.

References

[1] Yan C, Huang J, Sun K, et al. Cu_2ZnSnS_4 solar cells with over 10% power conversion efficiency enabled by heterojunction heat treatment. *Nature Energy*, **2018**, *3* (9): 764–772.

[2] Yang S C, Lin T Y, Ochoa M, et al. Efficiency boost of bifacial Cu(In, Ga)Se_2 thin-film solar cells for flexible and tandem applications with silver-assisted low-temperature process. *Nature Energy*, **2023**, *8* (1): 40–51.

[3] Burst J M, Duenow J N, Albin D S, et al. CdTe solar cells with open-circuit voltage breaking the 1 V barrier. *Nature Energy*, **2016**, *1* (3): 16015.

[4] Tang R F, Wang X M, Lian W T, et al. Hydrothermal deposition of antimony selenosulfide thin films enables solar cells with 10% efficiency. *Nature Energy*, **2020**, *5* (8): 587–595.

[5] Chen G J, Luo Y D, Abbas M, et al. Suppressing buried interface nonradiative recombination losses toward high-efficiency antimony triselenide solar cells. *Advanced Materials*, **2024**, *36* (5): 2308522.

[6] Chen S, Fu Y, Ishaq M, et al. Carrier recombination suppression and transport enhancement enable high-performance self-powered broadband Sb_2Se_3 photodetectors. *InfoMat*, **2023**, *5* (4): e12400.

[7] Tang R, Chen S, Zheng Z H, et al. Heterojunction annealing enabling record open-circuit voltage in antimony triselenide solar cells. *Advanced Materials*, **2022**, *34* (14): 2109078.

[8] Luo Y D, Chen G J, Chen S, et al. Carrier transport enhancement mechanism in highly efficient antimony selenide thin-film solar cell. *Advanced Functional Materials*, **2023**, *33* (14): 2213941.

[9] Chen X L, Che B, Zhao Y Q, et al. Solvent-assisted hydrothermal deposition approach for highly-efficient $Sb_2(S, Se)_3$ thin-film solar cells. *Advanced Energy Materials*, **2023**, *13* (21): 2300391.

[10] Li G, Dong J B, Xiao P, et al. Dual effect of NH_4F additive in the hydrothermal deposition of antimony selenosulfide thin film for high-performance solar cells. *Science China Materials*, **2022**, *65* (12): 3411–3417.

[11] Wang X M, Tang R F, Jiang C H, et al. Manipulating the electrical properties of $Sb_2(S, Se)_3$ film for high-efficiency solar cell. *Advanced Energy Materials*, **2020**, *10* (40): 2002341.

[12] Pan X Y, Pan Y L, Shen L Y, et al. All-vacuum-processed $Sb_2(S, Se)_3$ thin film photovoltaic devices via controllable tuning seed orientation. *Advanced Functional Materials*, **2023**, *33* (22): 2214511.

[13] Liu J J, Cao M S, Feng Z D, et al. Thermal evaporation–deposited hexagonal CdS buffer layer with improved quality, enlarged band gap, and reduced band gap offset to boost performance of $Sb_2(S, Se)_3$ solar cells. *Journal of Alloys and Compounds*, **2022**, *920* (1): 165885.

[14] Cheng J, Zhang Z, Zhao M H, et al. High-efficiency Sb_2Se_3 thin-film solar cells based on Cd(S, O) buffer layers prepared via spin-coating. *Materials Chemistry and Physics*, **2023**, *303* (1): 127794.

[15] Li K, Cai Z Y, Yang J J, et al. Molecular beam epitaxy deposition of in situ O-doped CdS films for highly efficient $Sb_2(S, Se)_3$ solar cells. *Advanced Functional Materials*, **2023**, *33* (48): 2304141.

[16] Schwartz C, Nordlund D, Weng T C, et al. Electronic structure study of the CdS buffer layer in CIGS solar cells by X-ray absorption spectroscopy: experiment and theory. *Solar Energy Materials and Solar Cells*, **2016**, *149* (1): 275–283.

[17] Ge J, Koirala P, Grice C R, et al. Oxygenated CdS buffer layers enabling high open-circuit voltages in earth-abundant Cu_2BaSnS_4 thin-film solar cells. *Advanced Energy Materials*, **2017**, *7* (6): 1601803.

[18] Guo L, Zhang B, Ranjit S, et al. Interface engineering via sputtered oxygenated CdS: O window layer for highly efficient Sb_2Se_3 thin-film solar cells with efficiency above 7%. *Solar RRL*, **2019**, *3* (10): 1900225.

[19] Hu X B, Tao J H, Wang Y Y, et al. 5.91%-efficient Sb_2Se_3 solar cells with a radio-frequency magnetron-sputtered CdS buffer layer. *Applied Materials Today*, **2019**, *16* (1): 367–374.

[20] Kephart J M, Geisthardt R M, Sampath W S. Optimization of CdTe thin-film solar cell efficiency using a sputtered, oxygenated CdS window layer. *Progress in Photovoltaics: Research and Applications*, **2015**, *23* (11): 1484–1492.

[21] Liu Y F, Li B, Liang X Y, et al. Reactively sputtered CdS: O buffer layers for substrate Sb_2Se_3 solar cells. *Journal of Alloys and Compounds*, **2023**, *932* (1): 167313.

[22] Ou C Z, Shen K, Li Z Q, et al. Bandgap tunable CdS: O as efficient electron buffer layer for high-performance Sb_2Se_3 thin film solar cells. *Solar Energy Materials and Solar Cells*, **2019**, *194*: 47–53.

[23] Paudel N R, Poplawsky J D, Moore K L, et al. Current enhancement of CdTe-based solar cells. *IEEE Journal of Photovoltaics*, **2015**, *5* (5): 1492–1496.

[24] Shiel H, Hutter O S, Phillips L J, et al. Natural band alignments and band offsets of Sb_2Se_3 solar cells. *ACS Applied Energy Materials*, **2020**, *3* (12): 11617–11626.

[25] Stoner J. What is Magnetron Sputtering and How Does it Work. **2022**. https://korvustech.com/magnetron-sputtering/#:~:text=The%20advantages%20of%20magnetron%20sputtering%20include%3A%201%20High,5%20Uniformity%20on%20large-area%20substrates%206%20Low%20temperature. Accessed December 26, 2023.

[26] Mchugh L F, Kumar P, Meendering D, et al. Method of making high-purity (>99%) MoO_2 powders, products made from MoO_2 powders, deposition of MoO_2 thin films, and methods of using such materials. Patent WO2005040044, **2005**.

[27] Wang K C, Shen P S, Li M H, et al. Low-temperature sputtered nickel oxide compact thin film as effective electron blocking layer for mesoscopic $NiO/CH_3NH_3PbI_3$ perovskite heterojunction solar cells. *ACS Applied Materials & Interfaces*, **2014**, *6* (15): 11851–11858.

[28] Wan L, Bai Z Z, Hou Z R, et al. Effect of $CdCl_2$ annealing treatment on thin CdS films prepared by chemical bath deposition. *Thin Solid Films*, **2010**, *518* (23): 6858–6865.

[29] Cai H L, Cao R, Gao J X, et al. Interfacial engineering towards enhanced photovoltaic performance of Sb_2Se_3 solar cell. *Advanced Functional Materials*, **2022**, *32* (46): 2208243.

[30] Yu M, Kenny S D. Using atomistic simulations to model cadmium telluride thin film growth. *Journal of Physics: Condensed Matter*, **2016**, *28* (10): 105002.

[31] de Assis T A, Aarão Reis F D A. Thin film deposition with time-varying temperature. *Journal of Statistical Mechanics: Theory and Experiment*, **2013**, *2013* (10): P10008.

[32] Blackwell S, Smith R, Kenny S D, et al. Modelling the growth of ZnO thin films by PVD methods and the effects of post-annealing. *Journal of Physics: Condensed Matter*, **2013**, *25* (13): 135002.

[33] Liu M, Man B Y, Lin X C, et al. Effect of temperature on pulsed laser deposition of HgCdTe films. *Applied Surface Science*, **2007**, *253* (24): 9291–9294.

[34] Kephart J M, McCamy J W, Ma Z, et al. Band alignment of front contact layers for high-efficiency CdTe solar cells. *Solar Energy Materials and Solar Cells*, **2016**, *157* (1): 266–275.

[35] Wetzelaer G A H, Kuik M, Nicolai H T, et al. Trap-assisted and Langevin-type recombination in organic light-emitting diodes. *Physical Review B*, **2011**, *83* (16): 165204.

[36] Wetzelaer G J A H, Scheepers M, Sempere A M, et al. Trap-assisted non-radiative recombination in organic–inorganic perovskite solar cells. *Advanced Materials*, **2015**, *27* (11): 1837–1841.

[37] Woo J C S, Plummer J D, Stork J M C. Non-ideal base current in bipolar transistors at low temperatures. *IEEE Transactions on*

DOI: 10.52396/JUSTC-2024-0048
JUSTC, **2024**, 54(6): 0604

Electron Devices, **1987**, *34* (1): 130–138.
[38] Kaminski A, Marchand J J, Laugier A. Non ideal dark I–V curves behavior of silicon solar cells. *Solar Energy Materials and Solar Cells*, **1998**, *51* (3/4): 221–231.
[39] Liang G X, Chen M D, Ishaq M, et al. Crystal growth promotion and defects healing enable minimum open-circuit voltage deficit in antimony selenide solar cells. *Advanced Science*, **2022**, *9* (9): 2105142.
[40] Ishaq M, Deng H, Yuan S J, et al. Efficient double buffer layer $Sb_2(Se_xS_{1-x})_3$ thin film solar cell via single source evaporation. *Solar RRL*, **2018**, *2* (10): 1800144.
[41] Zhao J, Li X R, Lin J H, et al. Unveiling the influence of absorber thickness on efficient $Sb_2(S, Se)_3$ solar cells through controlled chemical bath deposition. *Surfaces and Interfaces*, **2023**, *42* (1): 103411.
[42] Li J M, Zhao Y Q, Li C, et al. Hydrazine hydrate-induced surface modification of CdS electron transport layer enables 10.30%-efficient $Sb_2(S, Se)_3$ planar solar cells. *Advanced Science*, **2022**, *9* (25): 2202356.
[43] Sites J R, Mauk P H. Diode quality factor determination for thin-film solar cells. *Solar Cells*, **1989**, *27* (1): 411–417.
[44] Deng B Z, Lian H, Xue B T, et al. Niobium-carbide MXene modified hybrid hole transport layer enabling high-performance organic solar cells over 19%. *Small*, **2023**, *19* (23): 2207505.
[45] Lin Y R, Tunuguntla V, Wei S Y, et al. Bifacial sodium-incorporated treatments: Tailoring deep traps and enhancing carrier transport properties in Cu_2ZnSnS_4 solar cells. *Nano Energy*, **2015**, *16* (1): 438–445.
[46] Christians J A, Kamat P V. Trap and transfer. Two-step hole injection across the Sb_2S_3/CuSCN interface in solid-state solar cells. *ACS Nano*, **2013**, *7* (9): 7967–7974.
[47] Yang Z L, Wang X M, Chen Y Z, et al. Ultrafast self-trapping of photoexcited carriers sets the upper limit on antimony trisulfide photovoltaic devices. *Nature Communications*, **2019**, *10* (1): 4540.
[48] Guo H F, Chen Z W, Wang X, et al. Enhancement in the efficiency of Sb_2Se_3 thin-film solar cells by increasing carrier concertation and inducing columnar growth of the grains. *Solar RRL*, **2018**, *3* (3): 1800224.
[49] Li Z Q, Liang X Y, Li G, et al. 9.2%-efficient core-shell structured antimony selenide nanorod array solar cells. *Nature Communications*, **2019**, *10* (1): 125.
[50] Wu Q C, Lin X L, Mahabaduge H, et al. Effect of oxygen on the properties of CdSe thin films prepared by RF-sputtering. *Chemical Physics Letters*, **2022**, *799* (1): 139633.

DOI: 10.52396/JUSTC-2024-0048
JUSTC, **2024**, 54(6): 0604